A numerical investigation of the influence of the blade-vortex interaction on the dynamic stall onset in simplified rotor environment

Camille Castells, François Richez, Michel Costes

A Numerical Investigation of the Influence of the Blade-Vortex Interaction on the Dynamic Stall Onset in Simplified Rotor Environment

Camille Castells
PhD Student
ONERA, The French Aerospace lab
Meudon, France

François Richez
Research Scientist
ONERA, The French Aerospace lab
Meudon, France

Michel Costes
Research Scientist
ONERA, The French Aerospace lab
Meudon, France

ABSTRACT

Two- and three-dimensional models representative of a helicopter rotor blade element during forward flight have been implemented. The rotor blade element is considered in pitching oscillation motion with a non-uniform translation to take into account the speed variation in forward flight. Two stalled flight conditions of the 7A rotor have been selected in wind tunnel test data. These flight conditions have been investigated in a previous study and the aerodynamic behavior of the rotor blades in realistic rotor environment is known, including stall mechanisms. The capability of simplified models to reproduce the aerodynamic behavior of the blade element has been validated for a first case. Then, the influence of the blade-vortex interaction on stall onset has been investigated since the previous work on full articulated-rotor configurations does not allow to conclude on the role of the blade-vortex interaction on stall onset. The simplified models allow to isolate the influence of a vortex passing close to the blade element on aerodynamic loads. This work shows that a dynamic stall event is triggered in both cases while a vortex is passing close to the blade element. This clearly highlights that blade-vortex interaction can trigger stall in realistic rotor environment.

NOTATION

R	Rotor radius, m
c	Blade chord, m
ψ	Blade azimuthal position, deg
Ω	Rotational speed, rpm
M_{tip}	Tip Mach number
μ	Advance ratio
V_∞	Freestream velocity, ms^{-1}
σ	Rotor solidity
α_t	Shaft angle, deg
C_L/σ	Rotor lift coefficient
C_X/σ	Rotor propulsive force coefficient
M^2C_n	Section normal force coefficient
M^2C_m	Section pitching moment coefficient
θ	Section pitch angle, deg
θ_{elast}	Torsional deformation angle, deg
θ_0	Collective pitch angle, deg
θ_{1c}	Lateral cyclic pitch angle, deg
θ_{1s}	Longitudinal cyclic pitch angle, deg
β	Flap angle, deg
β_{1c}	Longitudinal flapping angle, deg
β_{1s}	Lateral flapping angle, deg
$K_p = -C_p$	Pressure coefficient
C_l	Section lift coefficient
V_{iz}	Vertical component induced by the induced velocity, ms^{-1}
α_i	Induced angle of attack, deg
$\alpha_{C_z=0}$	Zero-lift angle
Γ_{TV}	Circulation of the tip vortex emitted by the blade considered, m^2s^{-1}
Γ_{BVI}	Circulation of the vortex impacting the blade considered, m^2s^{-1}
ψ_{BVI}	Azimuthal position at BVI, deg
V_θ	Tangential velocity of the vortex, ms^{-1}
r_{core}	Vortex core radius, m
d	Vortex vertical distance from blade quarter chord at BVI, m

INTRODUCTION

Dynamic stall is a limiting phenomenon occurring during helicopter forward flight. It is due to high angles of attack, especially on the retreating blade side. It generates boundary layer separation, lift and pitching moment reductions at each rotor revolution. It causes vibrations and eventually can jeopardize the blade structure (Ref. 1). Therefore, it is essential to be able to understand its mechanisms in order to prevent it. Dynamic stall involves several mechanisms: three-dimensional unsteady separated flows, transonic flows including shocks, blade-vortex interactions (BVI), vortex shedding or fluid-structure coupling - to name just a few. Consequently, the dynamic stall remains challenging for

numerical prediction.

Historically, due to the dynamic stall complexity, most of the researches on dynamic stall were focused on two- and three-dimensional airfoil configurations in oscillating pitching motion. Indeed, McCroskey *et al.* in Ref. 2 showed that the angle of attack variation of a helicopter rotor blade element can be approximated by a *"large amplitude, low frequency sine wave"*. Several numerical (Refs. 3–6) and experimental (Refs. 7–12) studies have been dedicated to the understanding of the dynamic stall process on two-dimensional oscillating airfoils. McCroskey, Carr and McAlister (Refs. 7–9) highlighted the dynamic vortex shedding from leading edge to trailing edge during the stall process and the hysteresis aspect of the aerodynamic loads. They also investigated the capability of computational tools to predict stall through the influence of the grid size (Ref. 6, 13), the temporal resolution (Ref. 6, 14), the turbulent and transition modeling (Ref. 3, 5, 6, 15). Three-dimensional investigations on oscillating airfoils showed the influence of the finite span of the blade and the influence of the tip vortex on stall onset as Refs. 16–22. They highlighted that the tip vortex reduces the angle of attack near the tip and then delays the stall onset. Other studies considered the influence of the rotation and showed its great influence on the airloads (Refs. 23–28). The rotation kept the stall vortex closer to the blade surface compared to a non-rotating configuration.

However, the aerodynamic behavior of a rotor blade during a forward flight is more complicated than an airfoil in sine pitching oscillations in a uniform freestream flow. Loose coupling simulations between Computational Fluid Dynamic (CFD) and Comprehensive Analysis (CA) codes including the blade deformations and kinematics were developed to take into account all the phenomena which could appear in realistic rotor environment, notably in forward flight as presented in Ref. 29. This coupling strategy has shown to be able to predict the dynamic stall onset and its mechanisms on different stalled cases of rotor configurations in forward flight in several previous studies, among them, one can mention Refs. 30–36.

Consequently, the CDF/CA coupling procedure has been used to investigate deeply stall mechanisms in realistic rotor environment. Richez in Ref. 32 and then Castells *et al.* in Ref. 36 used coupling simulations between HOST (CA code) and elsA (CFD solver) to get a better understanding of the dynamic stall process for three forward flight conditions. The blade-vortex interaction has been pointed out as a possible trigger of the stall in these flight conditions. The angle of attack induced by the vortex is added to the local incidence of the blade due its motion and deformation. However, it was shown that, for the highest rotor thrust case investigated in Ref. 36, the stall onset occurs while the vortex has not yet reached the blade. Thus, it was not possible to attribute stall onset to blade vortex-interaction in this case.

Moreover, investigations have been made on the actual effect of the blade-vortex interaction on stall onset since the blade wake usually remains near the rotor disk in flight (Ref. 1). Landgrebe in Ref. 37 used experimental and theoretical studies of a NACA0012 four-bladed rotor in hover to evaluate the influence of the rotor wake on performances. The increase in thrust and thus in tip vortex circulation strength leads to increased local angle of attack values when the following blade is in the vicinity of this vortex. Thus, the angle of attack can reach a value involving dynamic stall. In Ref. 38, Gibertini *et al.* and Droandi *et al.*, in Ref. 39, highlighted, experimentally and numerically, that perpendicular blade-vortex interactions can be a trigger of dynamic stall. It increases locally the angle of attack on one side of the blade surface (where the vortex induces an upwash) promoting the flow separation and reduces it on the other side, delaying stall onset.

Thus, this work is dedicated to investigating more deeply the influence of the blade-vortex interaction on stall events in forward flight conditions. A numerical procedure had to be developed in order to isolate the blade-vortex interaction effect on the airloads, especially on dynamic stall, in realistic conditions. Consequently, the simplified model used to isolate the blade-vortex interaction event must reproduce, as close as possible, the behavior of a rotor blade element in rotor environment in forward flight.

EXPERIMENTAL DATA

An extensive database of the model-scale 7A rotor tested in the transonic closed-circuit S1MA wind tunnel at ONERA Modane test center, France, in 1991 (Ref. 40) is available. The 7A rotor is composed of four articulated blades of radius R = 2.1 m, constant chord c = 0.14 m and constant aerodynamic twist rate of -8.3 deg/R. The blade is made of two airfoils with a linear interpolation of the airfoil shape between them. A 13% relative thickness OA213 airfoil is used from inboard to 0.75R and a 9% relative thickness OA209 from 90% of the rotor radius to the tip. Figure 1 illustrates the 7A rotor mounted in the S1MA wind tunnel.

The experimental database provides unsteady pressure measurements and integrated sectional airloads at the five radial stations of the blade (r/R = 0.5, 0.7, 0.825, 0.915, and 0.975). Structural loads and blade motions are also available as blade bending moments, torsion moments, rigid angles and elastic deformations at sections r/R = 0.3, 0.4, 0.55, 0.65, 0.75 and 0.85.

In the present work, two forward flight conditions, referred to as LRPM and MRPM, have been selected. The selected flight conditions have the same propulsive and lift forces, only the rotor rotational speed (defined in revolutions per minute: RPM) is modified, changing the non-dimensional rotor load. The non-dimensional rotor load is increased as the RPM is reduced. These test cases have been deeply investigated by the authors in Ref. 36. Table 1 summarizes the flow parameters for each flight condition investigated. The two flight conditions are undergoing stall events and blade-vortex interaction seems to be involved in the stall process in at least one of the two cases (MPRM).

Table 1: Selected Flight Conditions (Ref. 36)

	Ω, rpm	M_{tip}	μ	C_L/σ	C_X/σ
Low RPM **LRPM**	964	0.616	0.315	0.11	0.0049
Moderate RPM **MRPM**	1022	0.646	0.3	0.1	0.0046

FULL ROTOR COMPUTATIONS

The authors, in Ref. 36, perfomed HOST/elsA coupling simulations on these two forward flight conditions. They highlighted that several dynamic stall events occured in these two flight conditions. The most severe one, the lowest RPM (referred to as LRPM), showed a double stall at the tip part of the blade as seen in Figure 2. The dynamic stall is defined by a sudden loss of lift and a sharp nose-down pitching moment on the retreating blade (180 deg $\leq \psi \leq$ 360 deg). They also showed that the blade-vortex interaction seems to be involved in the dynamic stall onset. At the blade tip, a small flow separation bubble appears at the leading edge for $210 \leq \psi \leq 270$ deg and this bubble bursts and leads to stall for the two test cases investigated in the present work. The stall onset, in this region, occurs at the blade vortex interaction azimuthal and radial position for the moderate RPM (MPRM) case as illustrated in Figure 3. However, in the lowest RPM (LRPM) flight case, the vortex is still far from the blade (estimated at 4 times the blade chord length) when the stall is initiated, also illustrated in Figure 3. Consequently, it is difficult to conclude on the effect of the blade-vortex interaction on the flow separation bubble bursting that leads to stall at the blade tip in this flow condition. Moreover, this complexity is increased as the blade also depends on several independent parameters such as the pitch and flap angles and torsional deflection.

The objective of this work is to define a simplified model representative of the behavior of a blade element in the selected flight conditions which can isolate the influence of the blade-vortex interaction on airloads and on dynamic stall occurence. This work will focus on the section at $r/R = 0.915$ (OA209 airfoil) since it was instrumented in the experiment and it was deeply investigated in Ref. 36. The simplified configurations developed allow us to compare at reduced cost the aerodynamic behavior of a rotor blade element with and without blade-vortex interaction by adding an analytical vortex similar to the one seen by the blade in rotor environment.

COMPUTATIONAL METHODOLOGY

Two simplified models representative of a blade element at the blade tip ($r/R = 0.915$) in the selected flight conditions have been implemented. The first one is a two-dimensional airfoil in translation and in pitch oscillation. An analytical vortex, based on the Scully vortex model (Ref. 41)) representative of the one encountered by the blade in rotor environment, obtained in full rotor computations, will be added in the simulations as illustrated in Figure 4. The second one is a three-dimensional model to investigate the influence of the three-dimensional effects (mostly finite-span features) on stall and on the blade-vortex interaction. It consists in a rotor blade element of finite span in translation and in pitch oscillation. Only the last 20% of the blade radius are kept since the dynamic stall, in these cases, is located in this region. These simulations will allow investigating the influence of the three-dimensional effects on dynamic stall.

Simulations are performed with the URANS finite volume elsA solver developed by ONERA (Ref. 42). A Chimera approach is done using the pre- and post-processing tool Cassiopee (Ref. 43) with near body structured grid around the rotor blade element and a background cartesian grid. A structured O-mesh around the airfoil has been used for the two-dimensional model (Figures 5) and a near body curvilinear structured grid around the blade tip have been extracted from the mesh used in Ref. 36 for the three-dimensional model (Figures 6). Consequently, the blade twist and the airfoil shape change (from OA213 to OA209) is included in the three-dimensional model. A particular attention has been made to maintain a similar mesh resolution as in Ref. 36 for the two-dimensional airfoil mesh.

The k-ω Kok (Ref. 44) turbulence model with the shear-stress transport (SST) correction is used to ensure consistency with the computations made in Ref. 36 which are used as reference. Moreover, all the numerical parameters are also chosen as identical to the ones used in the previous study. Thus, the time derivative is discretized with a second order implicit Gear scheme, at each time step, the non-linear problem is solved by an iterative Newton process. The time step is kept at $\Delta\psi = 0.225$ deg with 30 sub-iterations in the Newton iterative process.

The time- and CPU-cost have been widely reduced with respect to the full rotor simulation. The full rotor computation performed one rotor revolution in 200h using 250 CPUs while the 2D model needs 4h with 13 CPUs and the 3D model uses 222 CPUs during 20h to complete one rotor revolution (or 1600 iterations with the selected time step).

SIMPLIFIED ROTOR ENVIRONMENT MODELS

In this section, the simplified rotor environment models developed are presented. They consist in the representation of the rotor blade element as a two-dimensional airfoil or a three-dimensional blade tip in pitching oscillation and in translation.

Local Angle of Attack

The first step to model the behavior of a blade element in realistic rotor environment is to determine its effective incidence. It is not easy to extract the local angle of attack of a blade element from numerical simulations since it is strongly dependent on the induced velocity field, which has no straightforward definition in a real flow environment as it is based on Prandtl's model in the lifting line theory. Several methods to

compute this local angle of attack of the blade element, the section at $r/R = 0.915$, from the previous full rotor simulations have been tested. In this paper, only two of them are presented and compared.

Method 1: From Airloads One way to compute the angle of attack of the blade element is to use the airloads of the considered section from the previous CFD simulations presented in Ref. 36. The sectional angle of attack has been linked to the sectional load computed through airfoil polars. To simplify the calculation, the airfoil polar used is assumed to be fully linear :

$$\alpha = \frac{C_l\sqrt{1-M^2}}{2\pi} + \alpha_{C_z=0} \tag{1}$$

where C_l is the section lift coefficient, expressed in the local section frame (normal to the blade chord direction) and using $U = \Omega r + V_\infty.sin(\Omega t).cos(\alpha_t)$ as reference velocity, M is the local Mach number ($M = U/a$, with a is the speed of the sound) and $\alpha_{C_z=0}$ is the zero-lift angle.

The main drawback of this process is that the actual airfoil polar is not fully linear, a decrease of lift and of lift slope is observed at high angle of attack due to static stall. So, the linear approximation of lift may fail as soon as the angle of attack gets larger than the static stall angle. Consequently, the angle of attack will be underestimated when it exceeds this angle (α_{SS}), which mostly is the case when dealing with dynamic stall ($\alpha_{DS} \geq \alpha_{SS}$). Moreover, it is necessary to remove the effect of the previous blade tip vortex (included through the airloads) from the angle of attack to isolate its effects on the appearance of flow separation and stall. Thus, a filter is needed to remove the effect of the blade-vortex interaction and avoid the clear underestimation of the angle of attack due to the non-linearity of the airfoil aerodynamics polar at stall.

The blade-vortex interaction induced component of the angle of attack is assumed to have a strong high-frequency content since it occurs rapidly and briefly. Thus, only the first harmonic of the angle of attack computed from the full rotor simulation airloads was kept to model the pitch oscillations experienced by the rotor blade section without the blade-tip vortex effect. Figure 7 illustrates the azimuthal evolution of the angle of attack of the blade section for the MRPM case. It compares the angle of attack computed by HOST during the coupling procedure presented in Ref. 36 ($\alpha_{HOST/elsA}$), the angle of attack computed from the lift coefficient ($\alpha_{Airloads}$) and the angle of attack filtered ($\alpha_{1stHarmo}$). The high frequency variation between 270 deg $\leq \psi \leq$ 330 deg observed on the angle of attack computed by HOST and by the linear approximation have been filtered and the loss of angle of attack in this region of dynamic stall due to the linear approximation is also avoided. However, the filtered angle of attack is expected to be underestimated with respect to the effective angle of attack in realistic rotor environment of the rotor blade element considered. Moreover, if stall is not induced by the blade-vortex interaction, the filter does not allow to reproduce the overshoot of angle of attack in the stall region, which is assumed, at this point, to be induced by the blade-vortex interaction (highlighted in red in Figure 7).

Method 2: From Motion The second method is to compute the angle of attack of the blade element from the motion of the blade. The angle of attack of the blade element is split into three terms - the pitch angle defined by rotor trim θ, the torsional deformation θ_{elast} and the induced flow angle:

$$\alpha(r,\psi) = \theta + \theta_{elast} - arctan(U_P/U_T) \tag{2}$$

with :

$$\begin{cases} \theta(r,\psi) = \theta_0 + \theta_{1c}cos(\psi) + \theta_{1s}sin(\psi) + Twist \\ U_T(r,\psi) = \Omega r + V_\infty cos(\alpha_t)sin(\psi) \\ U_P(r,\psi) = (V_\infty sin\alpha_t + V_{iz})cos\beta + r\dot{\beta} + V_\infty cos\alpha_t cos\psi \sin\beta \end{cases}$$

The blade motions and elastic deformations come from HOST computation in the coupling procedure presented in Ref. 36. The main difficulty is to estimate the local induced velocity V_{iz} seen by the blade section. In this study, the induced velocity is computed with the semi-empirical formulation of Meijer-Drees (Ref. 45) :

$$V_{MD}(r,\psi) = \frac{F_Z/(2\rho_\infty\pi R^2)}{\Omega R(\mu - \frac{3}{2}\mu^3)}[1 + V_{MD,c}\frac{r}{R}cos\psi - V_{MD,s}\frac{r}{R}sin\psi]$$

with :

$$\begin{cases} V_{MD,c} = \frac{4}{3}(1 - 1.8\mu^2) \\ V_{MD,s} = 2\mu \end{cases}$$

A correction to take into account the deflection induced by the own tip vortex has also to be added $V_{iz} = V_{MD} + V_{TV}$. Indeed, the section considered is close to the blade tip. Thus, the influence of its own vortex emitted at the tip can modify the flow around the blade element investigated. The tip vortex is assumed to be similar to a semi-infinite straight vortex line. Moreover, the circulation is assumed to be constant along the vortex line and equal to the maximum of the radial blade bound circulation distribution at each time step. Consequently, the tip vortex induced velocity on a blade element at a radial position r is expressed as :

$$V_{TV}(r,\psi) = \frac{\Gamma_{TV}(\psi)}{4\pi(R-r)}$$

Figure 8 illustrates the azimuthal evolution of the angle of attack of the two-dimensional blade section for the MRPM case. It compares the angle of attack computed by HOST, the angle of attack computed from the lift coefficient and the angle of attack computed from the blade motion. The high frequency content observed in the stall region is not observed by the angle of attack computed here. It suggests, as expected, that the blade-vortex interaction can be involved in this sudden variation of the angle of attack.

This method has also been used for three-dimensional blade tip simulations since the influence of the tip vortex emitted by the blade element considered can be easily removed by setting $V_{TV}(r,\psi)=0$ in comparison with the first method based on the airloads: the influence of the tip vortex is, by definition, already included in the airloads. Indeed, the tip vortex influence is already taken into account in the three-dimensional model simulations since the blade tip is included. The blade element is of finite span and the tip vortex is emitted in these simulations.

Local freestream velocity

In this work, to reproduce the aerodynamic environment of a rotor blade in forward flight, the airspeed is chosen to be a combination of the rotating speed Ω and the advancing speed V_∞: $U=\Omega r+V_\infty.sin(\Omega t).cos(\alpha_t)$. Consequently, the airfoil or the blade tip is in non-uniform translation (Figure 4). However, no radial flow is implemented in the three-dimensional model while it can be expected to occur on the rotor blade due to blade rotation.

Tip Vortex and Blade-Vortex Interaction Characteristics

Then, the vortex impacting the section has to be characterized in order to obtain a blade-vortex interaction similar to the one observed in realistic rotor environment. The vortex will be defined in the CFD simulation using an analytical shape: the Scully vortex model (Ref. 41). Thus, to define the vortex, two parameters are needed: the vortex core radius r_{core} and the vortex strength Γ_{BVI}. The results of CFD/CA loose coupling simulation (Ref. 36) have been explored to quantify these vortex characteristics. To get the vortex core radius r_{core} and the vortex strength Γ_{BVI}, the velocity profile of the vortex has been extracted in a plane perpendicular to the vortex line close to the intersection in two orthogonal directions (X_0 and Z_0) as illustrated in Figure 9. However, the extraction must be made in a region were the tip vortex is only slightly perturbed by the blade. Consequently, it has been extracted earlier than the blade-vortex interaction but this is not a problem as the vortex circulation is conserved during its convection toward the blade.

Figure 10 illustrates the velocity profiles in both orthogonal directions for the MRPM case. The tangential velocity of the vortex V_θ is defined by the average of half the peak-to-peak value of the velocity in the two orthogonal directions: $V_{Z_0}(X_0)$ and $V_{X_0}(Z_0)$. The vortex core radius r_{core} is half the distance between the two extrema of the tangential velocity (Figure 10). As for the tangential velocity, V_θ, the vortex core radius is defined as the average of the values obtained in both orthogonal directions (X_0 and Z_0). Then, the vortex strength Γ_{BVI} can be deduced since the vortex maximum tangential velocity of the Scully model is defined as $V_\theta=\Gamma_{BVI}/(4\pi r_{core})$.

In order to obtain a similar blade-vortex interaction, the time ψ_{BVI} and the distance at the blade of the vortex when it interacts with the blade section d is also extracted from the previous CFD results (Figure 11). The interaction is defined by the vortex passing the quarter chord of the blade element considered ($r/R=0.915$).

The vortex can be included in computations by superposition of the velocity, the pressure and the density fields of the simplified computations without blade-vortex interaction and the ones obtained with the Scully vortex model as follows:

$$\begin{cases}\rho=\rho_{w/o\ BVI}+(\rho_{Scully}-\rho_\infty)\\ \vec{V}=\vec{V}_{w/o\ BVI}+\vec{V}_{Scully}\\ P=P_{w/o\ BVI}+(P_{Scully}-P_\infty)\end{cases}$$

SIMPLIFIED MODEL VALIDATION ON THE MRPM CASE

Validation of the 2D model

In this section, the two-dimensional models presented in the previous section will be validated on the MRPM case where the role of the BVI on stall triggering seemed to be clear in the full articulated-rotor simulation (Ref. 36). The two methods to compute the angle of attack of the blade section considered ($r/R=0.915$) are compared in order to investigate their capability to reproduce the behavior of this blade element in rotor environment. The vortex coming from the previous blade is added in the simulation as presented before to obtain an aerodynamic environment as close as possible to the rotor environment to allow comparison with the full articulated-rotor simulation and validation.

In Figure 12, the two laws of the angle of attack used (α_{Motion} and $\alpha_{1stHarmo}$) are presented and the vortex characteristics are shown in Table 2.

Table 2: Vortex Characteristics for the MRPM case

	V_θ, ms^{-1}	r_{core}, m	d, m	ψ_{BVI}, deg
Moderate RPM **MRPM**	25	0.055	-0.14	291

The sectional normal force coefficient M^2C_n at the considered section ($r/R=0.915$) computed from the full articulated-rotor simulation is compared to the ones obtained by the simplified two-dimensional models in Figure 13.

It can be noticed that the global trend is well reproduced by both models. However, the lift on the blade element in advancing blade, especially near $\psi=0$deg is overestimated in the two-dimensional simulation using α_{Motion}. It is likely due to the overestimation of the angle of attack in this region. Indeed, the rotor and the test stand wakes are convected and merged around $\psi=0$deg in rotor configuration (Figure 3). It modifies the aerodynamic environment and the local angle of attack but, in the model used to compute the angle of attack, the rotor and model support wake is not considered. It can lead to the overestimation of the angle of attack in this region.

The dynamic stall event around 270 deg $\leq \psi \leq$ 330 deg is however captured for both two-dimensional simulations. It is identified by the sudden loss of lift on the retreating blade. In both two-dimensional simulations, the dynamic stall is overestimated. Such kind of result has been observed in previous studies, two-dimensional configurations of dynamic stall are more intense than three-dimensional ones (Ref. 19). Costes *et al.* in Ref. 19 also highlighted that the two-dimensional numerical simulations causes earlier stall onset and later flow reattachment. In this study, the stall is fairly well predicted in terms of azimuthal phase (Figure 13).

However, the stall development computed from the airloads-based angle of attack ($\alpha_{1stHarmo}$) is slightly delayed with respect to the full HOST/*elsA* simulation. It is observed in Figure 14 representing the evolution of the pressure coefficient on the blade. Indeed, if the simulation using α_{Motion} shows a behavior in good agreement with the full rotor simulation but with overestimated stall effects, the simulation using $\alpha_{1stHarmo}$ shows a delay of more than $\Delta\psi = 5$ deg. It can also be noticed on the sectional normal force coefficient. The minimum of lift coefficient obtained with $\alpha_{1stHarmo}$ is delayed with respect to the two other simulations (2D model using α_{Motion} and full HOST/*elsA* simulation). This delay is most probably due to the underestimation of the angle of attack caused by the linear simplification made when computing $\alpha_{1stHarmo}$.

Thus, the formation of the dynamic stall vortex on the upper surface of the airfoil is also delayed in the simulation with $\alpha_{1stHarmo}$ while the simulation with α_{Motion} shows a better agreement with the full rotor configuration in Figures 15 and 16. This result was expected since a delay in airloads has been observed. The drop of lift is due to the convection of the dynamic stall vortex along the upper surface of the airfoil toward the trailing edge.

Validation of the 3D model

Three-dimensional simulations were made on the 7A rotor blade tip. We kept the last 20%R of the blade in order to allow 3D flows to develop and to influence dynamic stall. However, for the sake of compirison with two-dimensional simulations, the blade-vortex interaction is supposed to be parallel.

The angle of attack of the blade tip considered is computed using the second method (based on the blade motion) for two main reasons. First, it allows to easily remove the effect of its own tip vortex on the blade angle of attack ($V_{TV} = 0$). Second, the two-dimensional simulations showed a better agreement using this method with respect to the articulated-rotor simulated from Ref. 36 compared to the method using the linearized airloads.

It is clear that the angle of attack is dependent on the blade tip section radial position so a "twist law" would be necessary to reproduce properly the aerodynamic environment of the whole blade tip element. However, to reduce complexity and to compare with two-dimensional simulations, the angle of attack is supposed constant on the whole blade tip and equal to the angle of attack observed by the section considered ($r/R = 0.915$).

Figure 17 illustrates the angle of attack of the blade element considered in the three-dimensional computation compared to the one used in the two-dimensional computation in previous section with α_{Motion}. The difference is due to the blade twist of -3.615 deg at $r/R = 0.915$ (considered through the twisted blade tip geometry) and the removal of the blade's own tip vortex component on the induced velocity which must not be considered in 3D (Eq. 2).

Figure 18 compares the sectional normal force coefficient M^2C_n at the section ($r/R = 0.915$) of the full articulated-rotor simulation with the ones obtained by both simplified models. Once again the global trend is well reproduced by both models. The lift stall, characterized by the sharp loss of lift, is reduced when three-dimensional effects are considered. This behavior has been observed in previous studies. The three-dimensional investigation of stall leads to later stall onset compared to two-dimensional studies (Refs. 17–19) notably due to the tip vortex emitted by the blade and its interaction with the dynamic stall vortex. However, in Figure 19, the evolution of the pressure coefficient on the blade shows that, in three-dimensional simulations, the flow separation at the leading edge takes more time to be convected toward the trailing edge. Indeed, a small pressure "plateau" is observed at the leading edge in Figure 19 for 270 deg $\leq \psi \leq$ 280 deg which becomes large enough to reduce considerably the sectional lift at $\psi =$ 290 deg. The overshoot of pressure induced by the dynamic stall vortex is also less intense in the three-dimensional model compared to the two-dimensional model. The stall delay observed in the three-dimensional model simulations is also observed on the formation of the dynamic stall vortex on the upper surface in Figures 20 and 21.

ROLE OF THE BLADE-VORTEX INTERACTION ON STALL ONSET

In the previous section, the two simplified models using the angle of attack based on the blade motion showed a good agreement with the full articulated-rotor simulations. The aerodynamic behavior of the considered section ($r/R = 0.915$) is globally well predicted and the stall event for 270 deg $\leq \psi \leq$ 320 deg is captured. Consequently, these models will be used in this section to investigate the actual effect of the blade-vortex interaction with the preceding blade tip vortex on stall onset in both forward flight test cases. In order to investigate the effect of the blade-vortex interaction on stall onset, two computations will be compared: one with and the other without the vortex passing close to the blade element considered. Once again, both simplified models will be tested in both configurations.

Moderate RPM test case

In Ref. 36, the stall onset for the Moderate RPM flight condition was attributed to the blade-vortex interaction since the vortex coming from the preceding blade impacts the blade at

the azimuthal and radial position of the stall onset. The vortex induces an angle of attack variation on the blade when it is close and a sudden increase of the angle of attack is expected in the stall region.

The two-dimensional model simulations have been performed with and without an impacting vortex. The lift coefficient at section $r/R = 0.915$ computed from these simulations is plotted in Figure 22. A stall event with sharp loss of lift is obtained when the vortex is impacting the blade section while no stall is observed between 270 deg $\leq \psi \leq$ 320 deg when no blade-vortex interaction is implemented. This behavior clearly shows that the blade-vortex interaction is the trigger of dynamic stall in this flight condition. Three-dimensional blade tip simulations have also been performed to verify this conclusion. In Figure 23 the same outcome is observed, the stall event being triggered by the blade-vortex interaction at the considered section.

Low RPM test case

The main motivation of this research is that in Ref. 36 the stall onset for the Low RPM flight condition could not be clearly attributed to the blade-vortex interaction. In this flight condition, at stall onset, the vortex coming from the preceding blade is still distant from the blade of approximately $4c$ (in a constant radius surface). Consequently, the angle of attack induced by the vortex is expected to be lower and to affect less the section aerodynamics. However, Ref. 36 showed that in this flight conditions the angle of attack induced by the blade-vortex is not negligible in the stall region and that, coupled with high pitch angle, it can lead to stall.

The objective, here, is to use the simplified models presented previously to establish the effective role of the blade-vortex interaction on the stall onset in this flight condition.

Figure 24 represents the two angle of attack laws used to reproduce the aerodynamic environment of the blade element at $r/R = 0.915$ in realistic rotor environment. As expected, when Figures 17 and 24 are compared, the angle of attack is seen to be increased when the RPM is decreased at constant rotor lift and propulsive force (Ref. 36). It reaches an angle of attack of 14 deg at $\psi = 320$ deg in the 2D model for the LRPM case while the maximum does not exceed 12 deg in the MRPM fight condition. The vortex characteristics are shown in Table 3.

Table 3: Vortex Characteristics for the LRPM case

	V_θ, ms^{-1}	r_{core}, m	d, m	ψ_{BVI}, deg
Low RPM **LRPM**	25	0.05	-0.14	293

As for the MPRM case, two-dimensional model simulations have been performed with and without an impacting vortex. Figure 25 represents the lift coefficient at section $r/R = 0.915$. Without impacting vortex (red line in Figure 25), no stall event is observed between 270 deg $\leq \psi \leq$ 320 deg but a lift stall is obtained around $\psi = 330$ deg which seems to reproduce the second stall event in the full articulated-rotor simulations. However, when a blade-vortex interaction is implemented in the computation (green line in Figure 25), a strong and sharp stall event is obtained in azimuthal phase with the one in full articulated-rotor simulation. The second stall event is missed in this simulation probably due to the passing vortex reducing angle of attack while leaving the trailing edge. Moreover, in Ref. 36, a second blade-vortex interaction is highlighted around $\psi = 330$ deg which is not implemented in this work. This second blade-vortex interaction can modify the airfoil behavior in the second stall region around $\psi = 330$ deg.

Figure 26 illustrates the section lift coefficient at section $r/R = 0.915$ in the three-dimensional blade tip simulation. The conclusions are the same as for the MRPM case, with the exception of the second stall event which is completely missed. The stall event is, as in the MRPM case, delayed when the three-dimensional effects are considered.

CONCLUSIONS

The main conclusions drawn from this work are as follows:

- Two- and three-dimensional simplified models representative of the aerodynamic behavior of a rotor blade element in forward flight have been implemented.
- Both simplified models have shown satisfactory agreement with the reference simulation of a full-articulated and deformable helicopter rotor in forward flight.
- The time-cost of the simulations has been considerably reduced compared to full-articulated and deformable rotor simulations.
- Simplified models have been used to isolate the blade-vortex interaction effect on stall onset of an airfoil and a finite blade tip in pitching oscillation motion and in translation.
- Blade-vortex interaction is a trigger of dynamic stall in both flight conditions considered.

However, in this work only parallel blade-vortex interactions are considered while in realistic rotor environment in the flight conditions investigated the interaction is oblique (Ref. 36). It can be a natural continuation of this work to investigate this feature of the interaction on stall onset and stall intensity. Moreover, these simplified models could also be used to perform comparative studies of the effect of blade-vortex interaction features on stall or to perform an optimization of the blade geometry to withstand the blade-vortex interaction induced stall.

Author contact: Camille Castells camille.castells@onera.fr

ACKNOWLEDGMENTS

Part of this research was supported by a DGA scholarship.
The studies presented in this article are making use of the elsA-ONERA software, whose co-owners are Airbus, Safran, and ONERA.

REFERENCES

1. G. J. Leishman, *Principles of Helicopter Aerodynamics*. Cambridge aerospace series, Cambridge University Press, 2006.

2. W. J. McCroskey and R. K. Fisher, "Detailed Aerodynamic Measurements on a Model Rotor in the Blade Stall Regime," *Journal of the American Helicopter Society*, vol. 17, pp. 20–30, Jan. 1972. DOI: 10.4050/jahs.17.1.20.

3. G. R. Srinivasan, J. A. Ekaterinaris, and W. J. McCroskey, "Evaluation of Turbulence Models for Unsteady Flows of an Oscillating Airfoil," *Computers & Fluids*, vol. 24, pp. 833 – 861, Sept. 1995. DOI: 10.1016/0045-7930(95)00016-6.

4. J. A. Ekaterinaris and M. F. Platzer, "Computational Prediction of Airfoil Dynamic Stall," *Progress in Aerospace Sciences*, vol. 33, pp. 759 – 846, Apr. 1998. DOI: 10.1016/S0376-0421(97)00012-2.

5. M. Costes, V. Gleize, A. Le Pape, and F. Richez, "Numerical Investigation of Laminar/Turbulent Transition Effects on the Dynamic Stall of an Oscillating Airfoil," in *American Helicopter Society 4th Decennial Specialist's Conference on Aeromechanics, San Francisco, CA*, 2008.

6. K. Richter, A. Le Pape, T. Knopp, M. Costes, V. Gleize, and A. D. Gardner, "Improved Two-Dimensional Dynamic Stall Prediction with Structured and Hybrid Numerical Methods," *Journal of the American Helicopter Society*, vol. 56, pp. 1–12, Oct. 2011. DOI: 10.4050/JAHS.56.042007.

7. W. J. McCroskey, L. W. Carr, and K. W. McAlister, "Dynamic Stall Experiments on Oscillating Airfoils," *AIAA Journal*, vol. 14, pp. 57–63, Jan. 1976. DOI: 10.2514/3.61332.

8. L. W. Carr, K. W. McAlister, and W. J. McCroskey, "Analysis of the development of dynamic stail based on oscillating airfoil experiments," tech. rep., NASA TN D-8382, 1977.

9. W. J. McCroskey, "Unsteady Airfoils," *Annual Review of Fluid Mechanics*, vol. 14, pp. 285–311, Jan. 1982. DOI: 10.1146/annurev.fl.14.010182.001441.

10. R. A. Piziali, "2D and 3D Oscillating Wing Aerodynamics for a Range of Angles of Attack Including Stall.," tech. rep., NASA Technical Memorandum 4632, 1994.

11. K. Mulleners and M. Raffel, "The Onset of Dynamic Stall Revisited," *Experiments in Fluids*, vol. 52, pp. 779–793, Mar 2012. DOI: 10.1007/s00348-011-1118-y.

12. K. Mulleners and M. Raffel, "Dynamic Stall Development," *Experiments in Fluids*, vol. 54, Feb. 2013. DOI: 10.1007/s00348-013-1469-7.

13. M. Costes, V. Gleize, J. Szydlowski, L. Sankar, G. Guzel, and M. Rhee, "Grid Sensitivity Study for the Turbulent Viscous Flow around a NACA 0015 Airfoil at Stall," in *31stEuropean Rotorcraft Forum, Florence*, Sept. 2005.

14. N. D. Liggett and M. J. Smith, "Temporal Convergence Criteria for Time-Accurate Viscous Simulations of Separated Flows," *Computers & Fluids*, vol. 66, pp. 140–156, Aug. 2012. DOI: 10.1016/j.compfluid.2012.06.010.

15. K. Richter, S. Koch, A. D. Gardner, H. Mai, A. Klein, and C. H. Rohardt, "Experimental Investigation of Unsteady Transition on a Pitching Rotor Blade Airfoil," *Journal of the American Helicopter Society*, vol. 59, pp. 1–12, Jan. 2014. DOI: 10.4050/jahs.59.012001.

16. P. Lorber, A. C. Jr., and F. Carta, "Dynamic Stall Experiments on a Swept Three-Dimensional Wing in Compressible Flow," in *22nd Fluid Dynamics, Plasma Dynamics and Lasers Conference*, American Institute of Aeronautics and Astronautics, June 1991. DOI: 10.2514/6.1991-1795.

17. A. Spentzos, G. Barakos, K. Badcock, B. Richards, P. Wernert, S. Schreck, and M. Raffel, "Investigation of Three-Dimensional Dynamic Stall Using Computational Fluid Dynamics," *AIAA Journal*, vol. 43, pp. 1023–1033, May 2005. DOI: 10.2514/1.8830.

18. A. Le Pape, G. Pailhas, F. David, and J.-M. Deluc, "Extensive Wind Tunnel Tests Measurements of Dynamic Stall Phenomenon for the OA209 Airfoil Including 3D Effects," in *33rd European Rotorcraft Forum, Kazan, Russia*, 2007.

19. M. Costes, F. Richez, A. Le Pape, and R. Gavériaux, "Numerical Investigation of Three-Dimensional Effects during Dynamic Stall.," in *37th European Rotorcraft Forum, Milan, Italy*, 2011.

20. V. Raghav and N. Komerath, "Velocity measurements on a retreating blade in dynamic stall," *Experiments in Fluids*, vol. 55, Feb. 2014. DOI: 10.1007/s00348-014-1669-9.

21. T. Schwermer, A. D. Gardner, and M. Raffel, "Dynamic Stall Experiments on a Rotor with High Cyclic Setting in Axial Inflow," in *73rd American Helicopter Society International Annual Forum and Technology Display, Fort Worth, TX*, 2017.

22. T. Schwermer, A. D. Gardner, and M. Raffel, "A Novel Experiment to Understand the Dynamic Stall Phenomenon in Rotor Axial Flight," *Journal of the American Helicopter Society*, vol. 64, pp. 1–11, Jan. 2019. DOI: 10.4050/jahs.64.012004.

23. H. a. Himmelskamp, *Profile Investigations on a Rotating Airscrew*. ARC-10856, Ministry of Aircraft Production, 1947.

24. V. Raghav and N. Komerath, "Dynamic Stall Life Cycle on a Rotating Blade in Steady Forward Flight," *Journal of the American Helicopter Society*, vol. 60, pp. 1–12, July 2015. DOI: 10.4050/jahs.60.032007.

25. V. Raghav and N. Komerath, "Advance ratio effects on the flow structure and unsteadiness of the dynamic-stall vortex of a rotating blade in steady forward flight," *Physics of Fluids*, vol. 27, p. 027101, Feb. 2015. DOI: 10.1063/1.4906803.

26. H. Dumitrescu and V. Cardos, "Inboard Stall Delay due to Rotation," *Journal of Aircraft*, vol. 49, pp. 101–107, Jan. 2012. DOI: 10.2514/1.c031329.

27. K. Mulleners, K. Kindler, and M. Raffel, "Dynamic Stall on a Fully Equipped Helicopter Model," *Aerospace Science and Technology*, vol. 19, pp. 72–76, June 2012. DOI: 10.1016/j.ast.2011.03.013.

28. A. D. Gardner and K. Richter, "Influence of Rotation on Dynamic Stall," *Journal of the American Helicopter Society*, vol. 58, pp. 1–9, July 2013. DOI: 10.4050/jahs.58.032001.

29. M. Potsdam, H. Yeo, and W. Johnson, "Rotor Airloads Prediction Using Loose Aerodynamic/Structural Coupling," *Journal of Aircraft*, vol. 43, pp. 732–742, May 2006. DOI: 10.2514/1.14006.

30. B. Ortun, M. Potsdam, H. Yeo, and K. V. Truong, "Rotor Loads Prediction on the ONERA 7A Rotor Using Loose Fluid/Structure Coupling," *Journal of the American Helicopter Society*, vol. 62, pp. 1–13, July 2017. DOI: 10.4050/jahs.62.032005.

31. F. Richez and B. Ortun, "Numerical Investigation of the Flow Separation on a Helicopter Rotor in Dynamic Stall Configuration," in *42nd European Rotorcraft Forum, Lille, France*, 2017.

32. F. Richez, "Analysis of Dynamic Stall Mechanisms in Helicopter Rotor Environment," *Journal of the American Helicopter Society*, vol. 63, pp. 1–11, Apr. 2018. DOI: 10.4050/jahs.63.022006.

33. N. M. Chaderjian, "Navier-Stokes Simulation of UH-60A Rotor/Wake Interaction Using Adaptive Mesh Refinement," in *73rd American Helicopter Society International Annual Forum and Technology Display, Fort Worth, TX*, 2017.

34. A. L. Grubb, C. Castells, R. Jain, F. Richez, and M. J. Smith, "High Fidelity CFD Analyses of Dynamic Stall on a Four-Bladed Fully Articulated Rotor System," in *74th American Helicopter Society International Annual Forum and Technology Display, Phoenix, AZ*, 2018.

35. F. Richez, "Numerical Analysis of Dynamic Stall for Different Helicopter Rotor Flight Conditions," in *73rd American Helicopter Society International Annual Forum and Technology Display, Fort Worth, TX*, 2017.

36. C. Castells, F. Richez, and M. Costes, "Numerical Analysis of RPM effect on Dynamic Stall Phenomena on Helicopter Rotor at High Thrust Forward Flight," *75th Vertical Flight Society Annual Forum, At Philadelphia, Pennsylvania, USA*, May 2019.

37. A. J. Landgrebe, "The wake geometry of a hovering helicopter rotor and its influence on rotor performance," *Journal of the American Helicopter Society*, vol. 17, pp. 3–15, Oct. 1972. DOI: 10.4050/jahs.17.4.3.

38. G. Gibertini, A. Mencarelli, and A. Zanotti, "Oscillating Aerofoil and Perpendicular Vortex Interaction," *Proceedings of the Institution of Mechanical Engineers, Part G: Journal of Aerospace Engineering*, vol. 228, pp. 846–858, Apr. 2013. DOI: 10.1177/0954410013481154.

39. G. Droandi, G. Gibertini, and A. Zanotti, "Perpendicular BladeVortex-Interaction over an Oscillating Airfoil in Light Dynamic Stall," *Journal of Fluids and Structures*, vol. 65, pp. 472–494, 07 2016. DOI: 10.1016/j.jfluidstructs.2016.07.010.

40. P. Crozier, "Recent Improvements in Rotor Testing Capabilities in the ONERA S1MA Wind Tunnel.," in *20th European Rotorcraft Forum, Amsterdam, Netherlands,*, 1994.

41. M. G. Scully, "Computation of helicopter rotor wake geometry and its influence on rotor harmonic airloads," tech. rep., PhD Thesis, Massachussets Institute of Technology, 1975.

42. L. Cambier, S. Heib, and S. Plot, "The ONERA elsA CFD Software: Input from Research and Feedback from Industry," *Mechanics & Industry*, vol. 14, no. 3, pp. 159–174, 2013. DOI: 10.1051/meca/2013056.

43. C. Benoit, S. Péron, and S. Landier, "Cassiopee: A CFD Pre- and Post-Processing Tool," *Aerospace Science and Technology*, vol. 45, pp. 272–283, Sept. 2015. DOI: 10.1016/j.ast.2015.05.023.

44. J. C. Kok, "Resolving the Dependence on Freestream Values for the k- ω Turbulence Model," *AIAA Journal*, vol. 38, pp. 1292–1295, July 2000. DOI: 10.2514/2.1101.

45. J. Meijer-Drees, "A theory of airflow through rotors and its application to some helicopter problems," *Journal of the Helicopter Association of Great Britain*, vol. 3, no. 2, pp. 79–104, 1949.

Figure 1: 7A rotor in ONERA Modane S1MA Wind Tunnel.

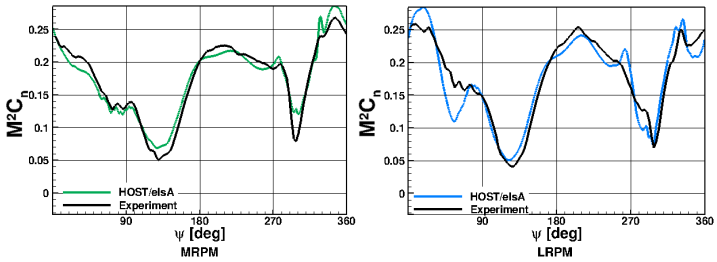

a) Sectional normal force coefficient

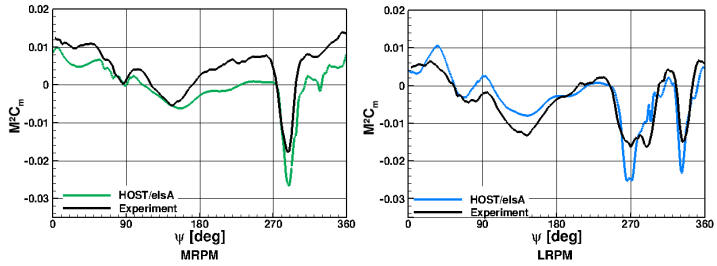

b) Sectional pitching moment coefficient

Figure 2: Sectional airloads at section $r/R = 0.915$ for both cases by coupling simulations (Ref. 36).

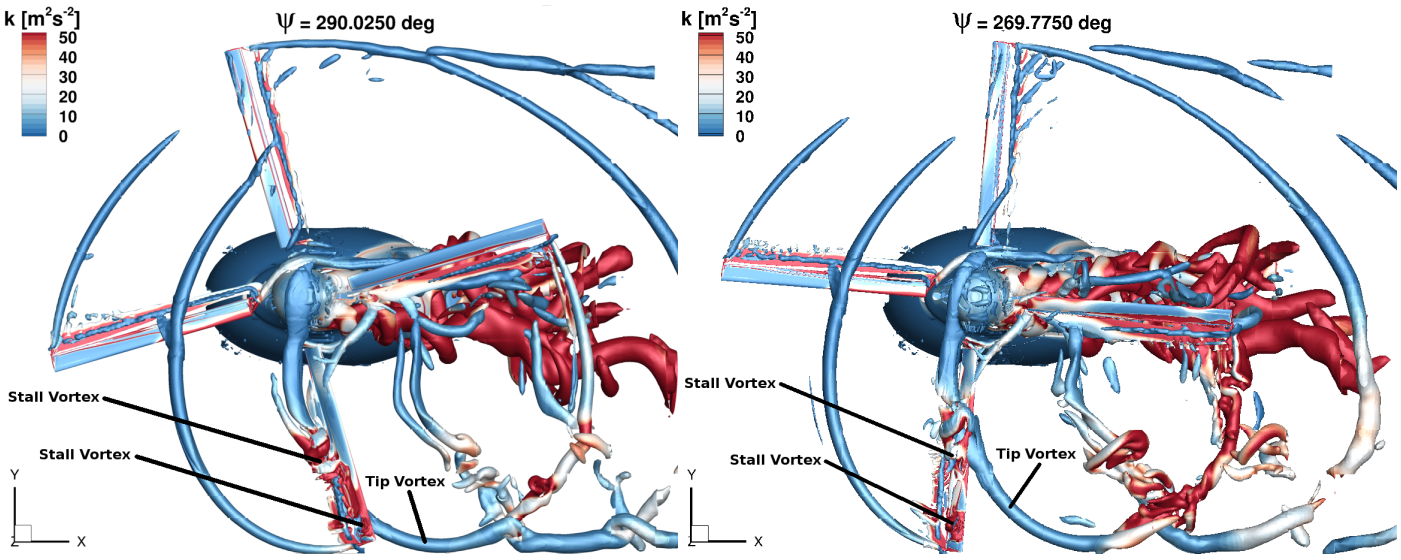

a) MRPM *b) LRPM*

Figure 3: Isocontour of Q criterion colored by the turbulent kinetic energy for the blade at the azimuthal position of the minimum of M^2C_m associated to the event in flow-separation region B (Ref. 36).

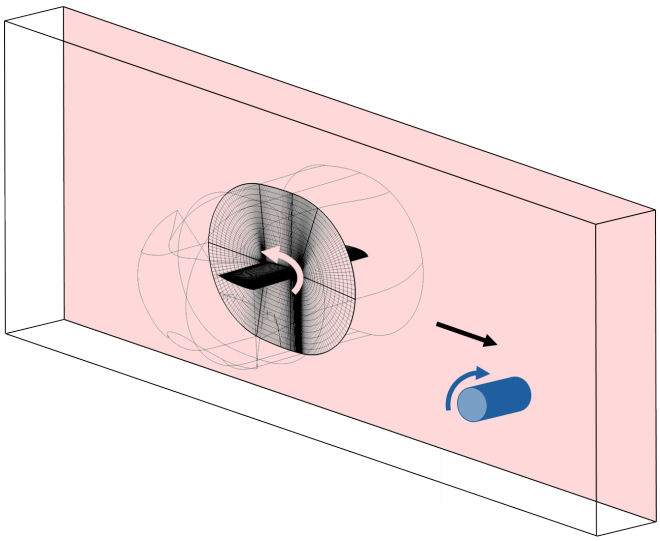

Figure 4: Schematic drawing of the simplified model used to isolate BVI effect on stall.

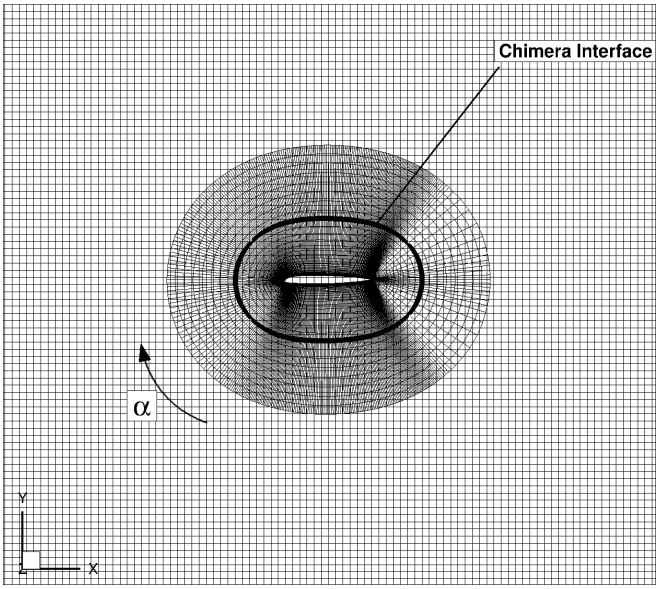

Figure 5: Two-dimensional structured mesh around a OA209 airfoil.

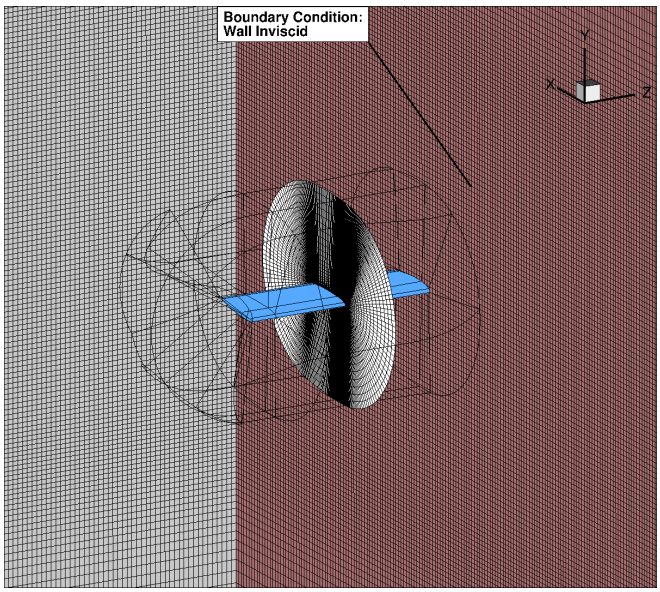

Figure 6: Three-dimensional structured mesh around a 7A rotor blade tip.

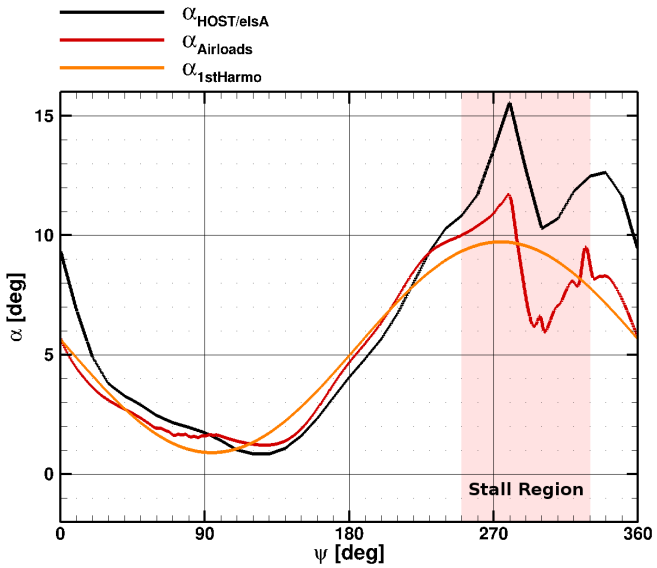

Figure 7: Extraction of the angle of attack of the blade section from the lift coefficient (MRPM).

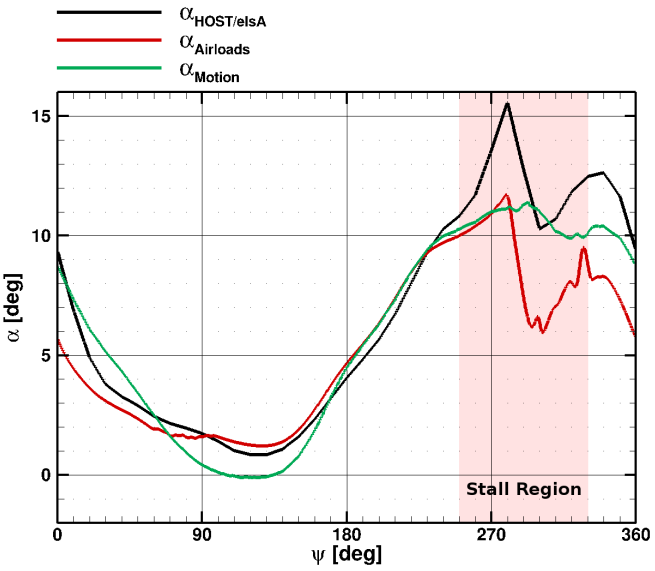

Figure 8: Extraction of the angle of attack of the blade section from the motion of the blade (MRPM).

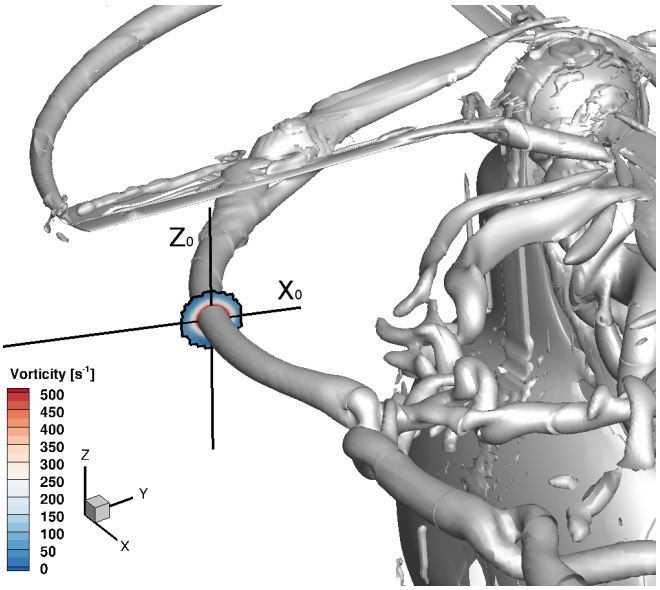

Figure 9: Determination of the vortex characteristics in a plane perpendicular to the vortex line (MRPM).

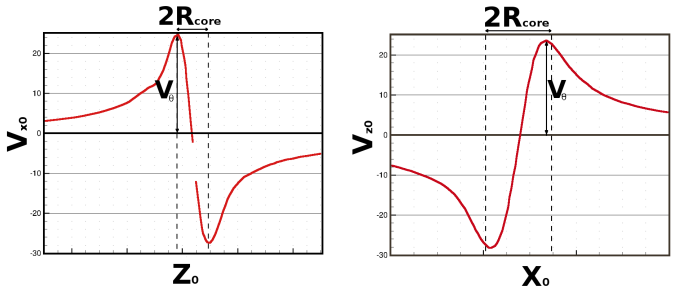

Figure 10: Extraction of V_θ and r_{core} (MRPM).

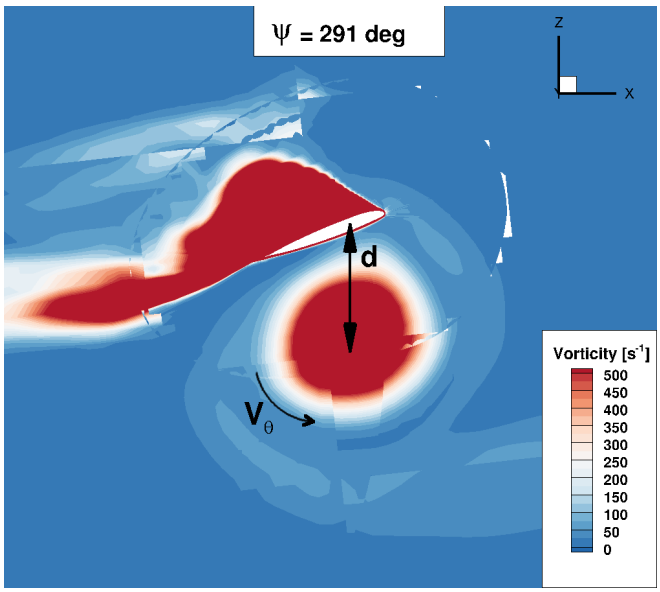

Figure 11: Determination of the azimuthal position at tip vortex "impact" (MRPM).

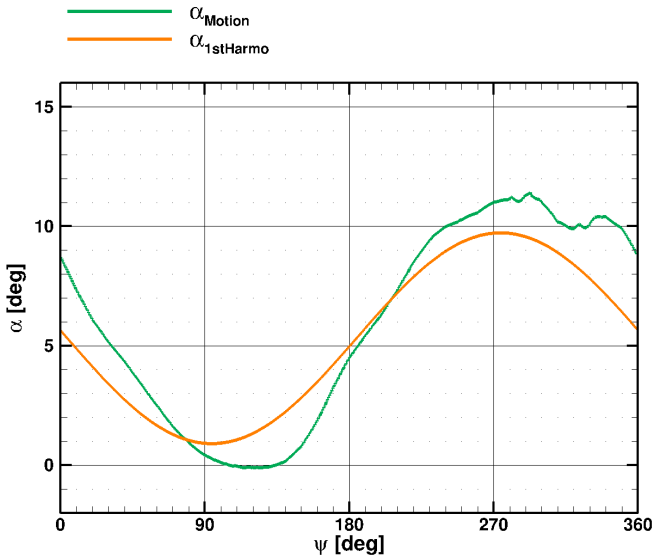

Figure 12: Angle of attack of the MRPM case from the two methods.

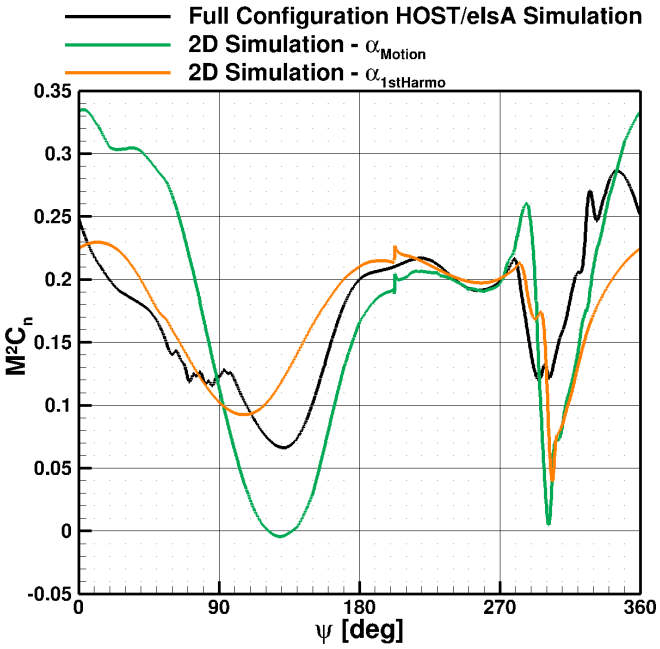

Figure 13: Sectional normal force coefficient of the MRPM case. Comparison of the laws of angle of attack used.

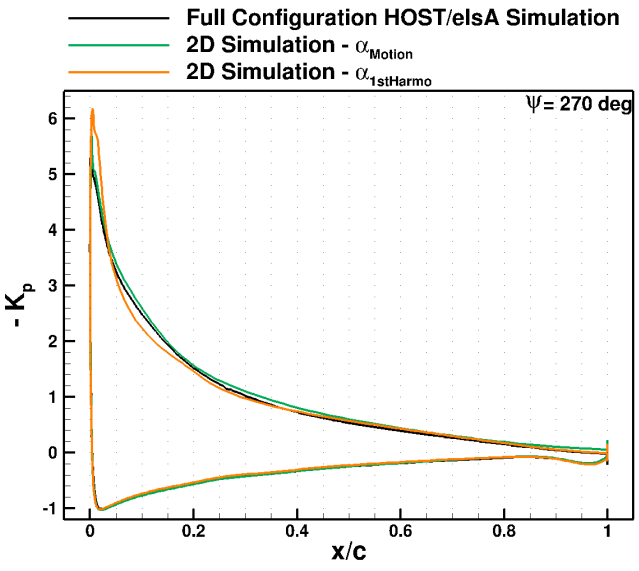

a) $\psi = 270\,\text{deg}$

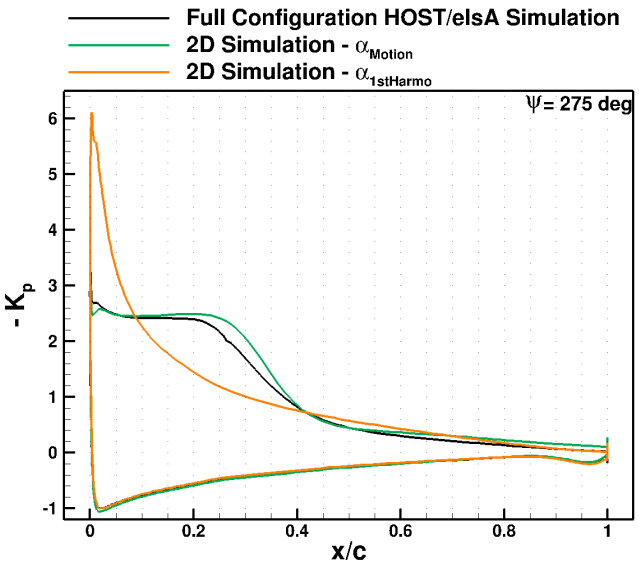

b) $\psi = 275\,\text{deg}$

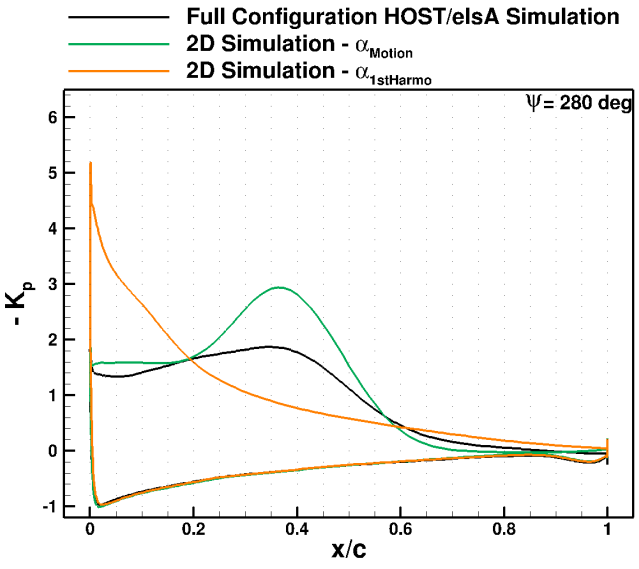

c) $\psi = 280\,\text{deg}$

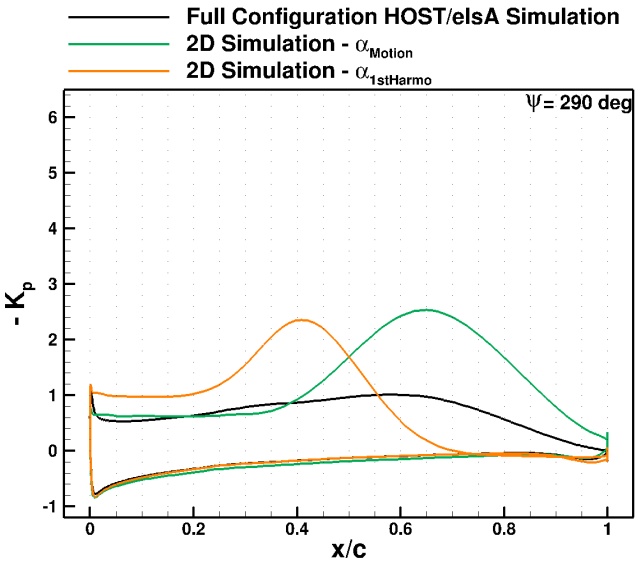

d) $\psi = 290\,\text{deg}$

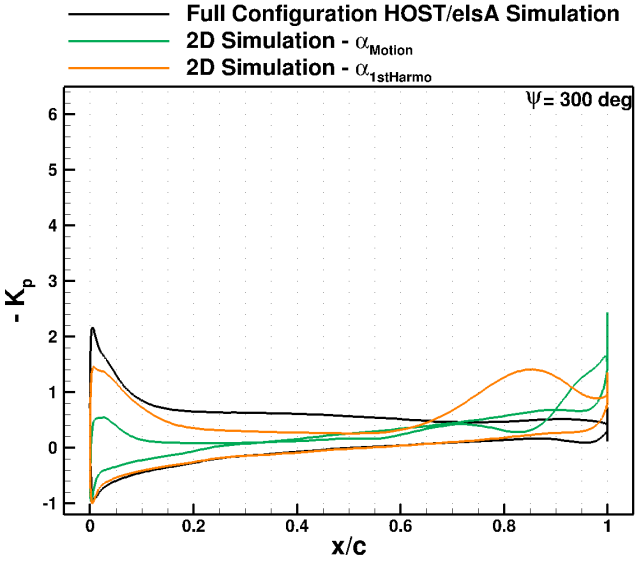

e) $\psi = 300\,\text{deg}$

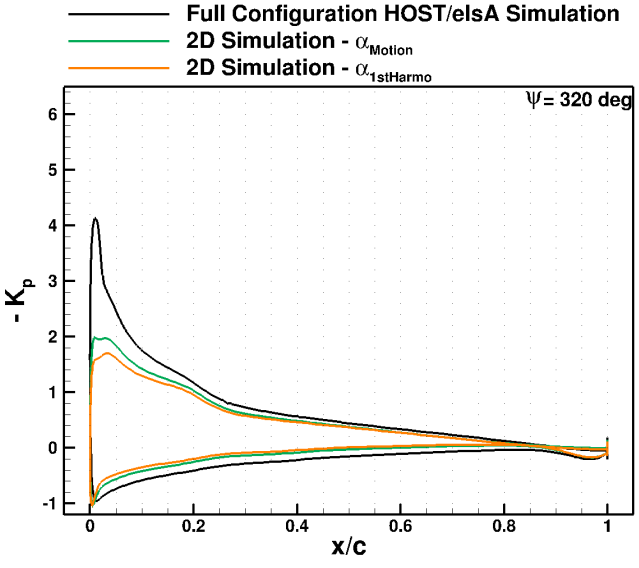

f) $\psi = 320\,\text{deg}$

Figure 14: Pressure coefficient at several azimuthal positions of the blade. 2D Simulations (MRPM).

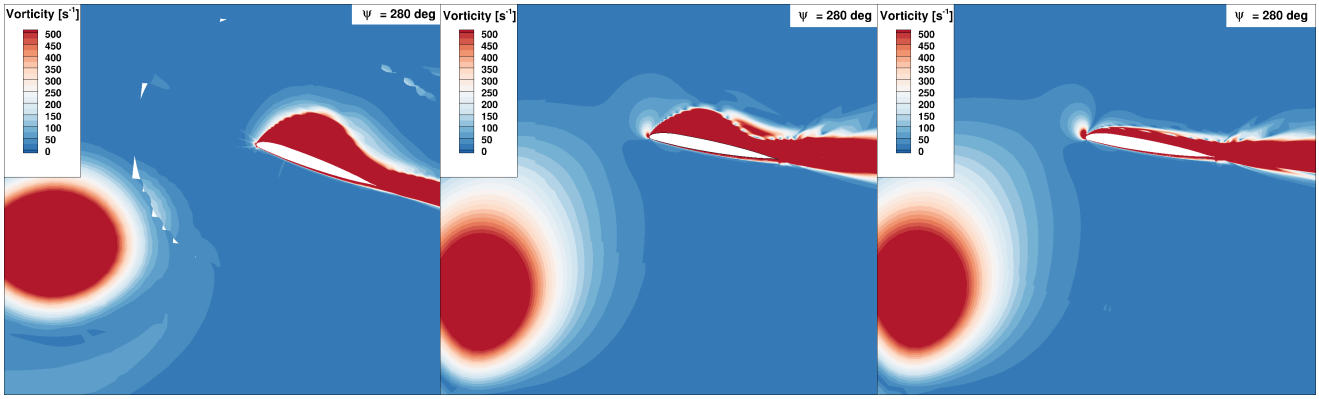

a) 3D HOST/*elsA* Simulation **b) 2D Simulation - α_{Motion}** **c) 2D Simulation - $\alpha_{1stHarmo}$**

Figure 15: Vorticity field at $\psi = 280\,\text{deg}$ (MRPM).

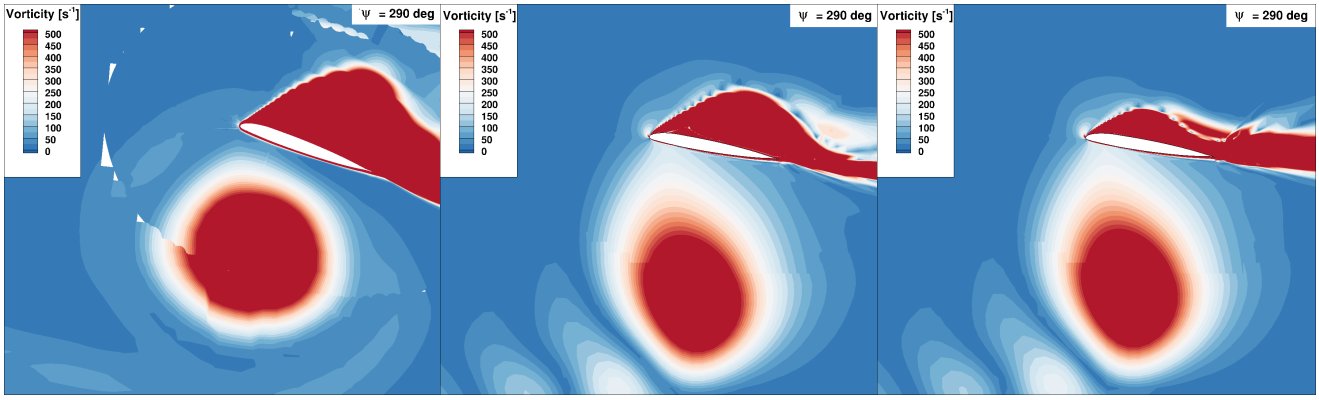

a) 3D HOST/*elsA* Simulation **b) 2D Simulation - α_{Motion}** **c) 2D Simulation - $\alpha_{1stHarmo}$**

Figure 16: Vorticity field at $\psi = 290\,\text{deg}$ (MRPM).

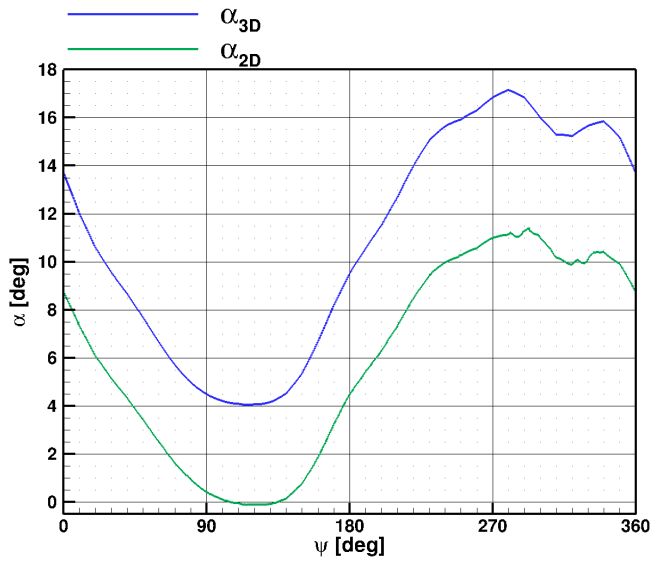

Figure 17: Angle of attack of the MRPM case used in 2D and 3D simulations.

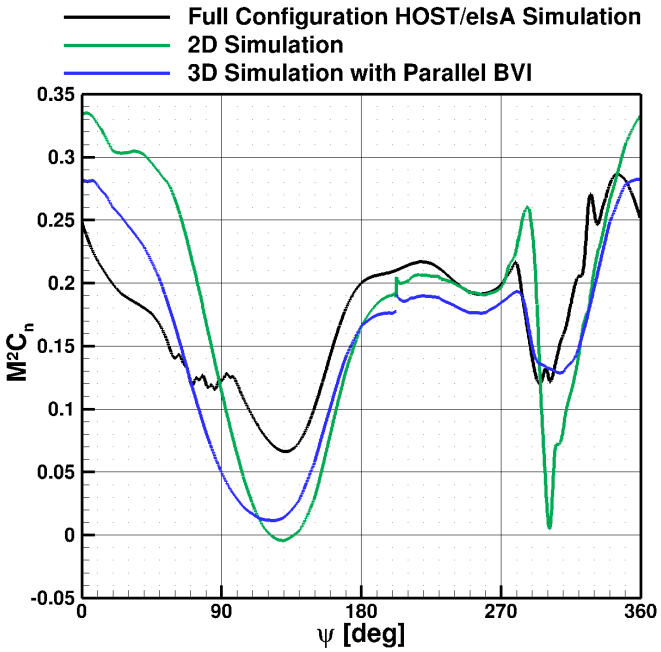

Figure 18: Sectional normal force coefficient of the MRPM case using 2D and 3D simulations.

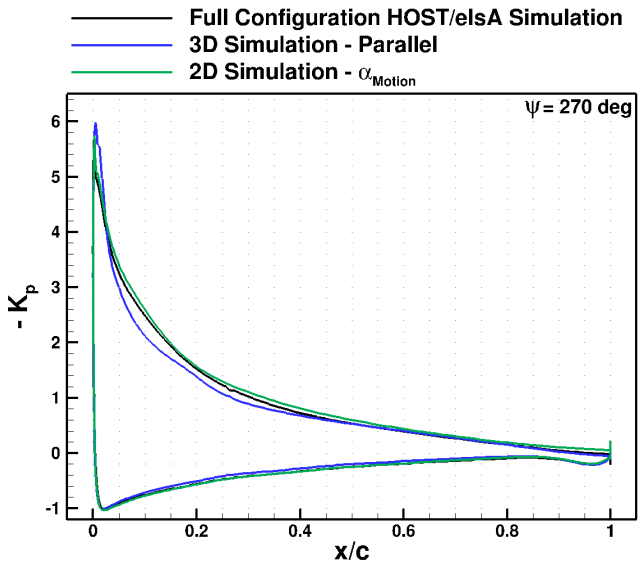

a) $\psi = 270\,\mathrm{deg}$

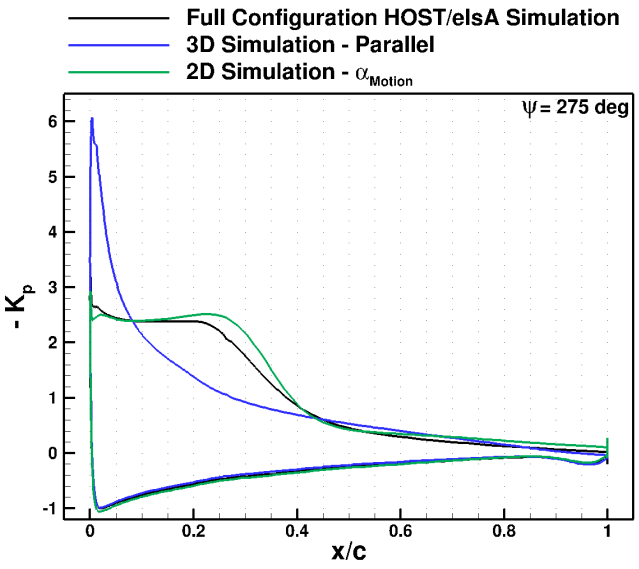

b) $\psi = 275\,\mathrm{deg}$

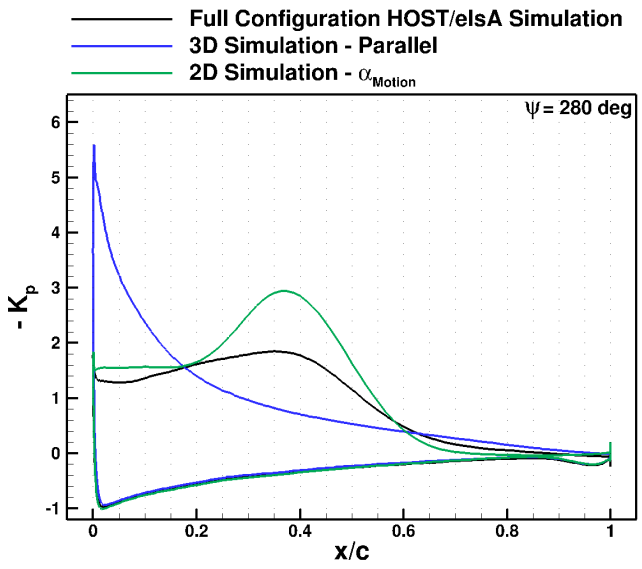

c) $\psi = 280\,\mathrm{deg}$

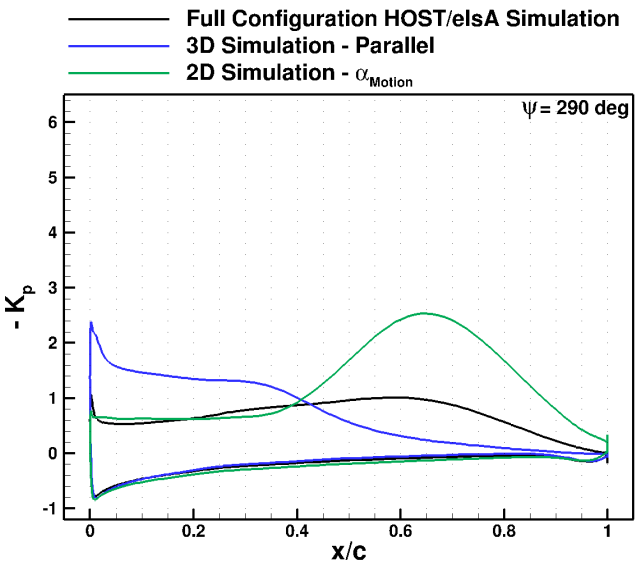

d) $\psi = 290\,\mathrm{deg}$

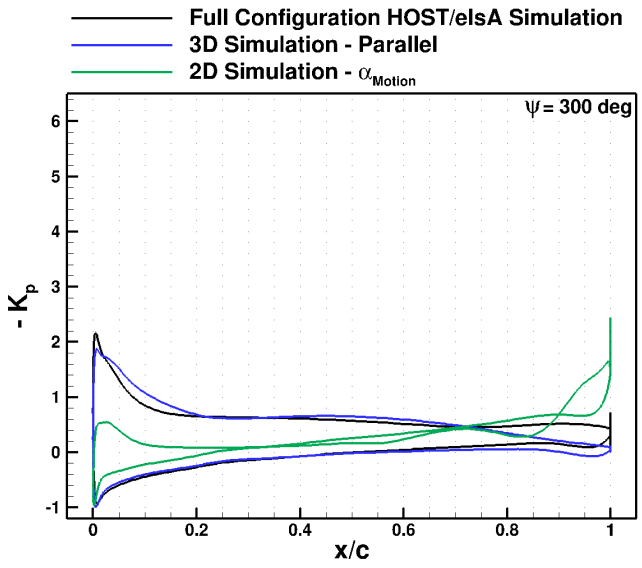

e) $\psi = 300\,\mathrm{deg}$

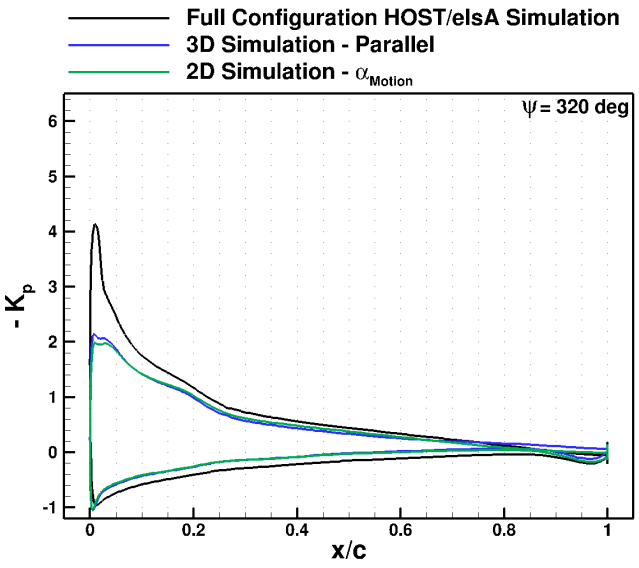

f) $\psi = 320\,\mathrm{deg}$

Figure 19: Pressure coefficient at several azimuthal positions of the blade. 3D Simulations (MRPM).

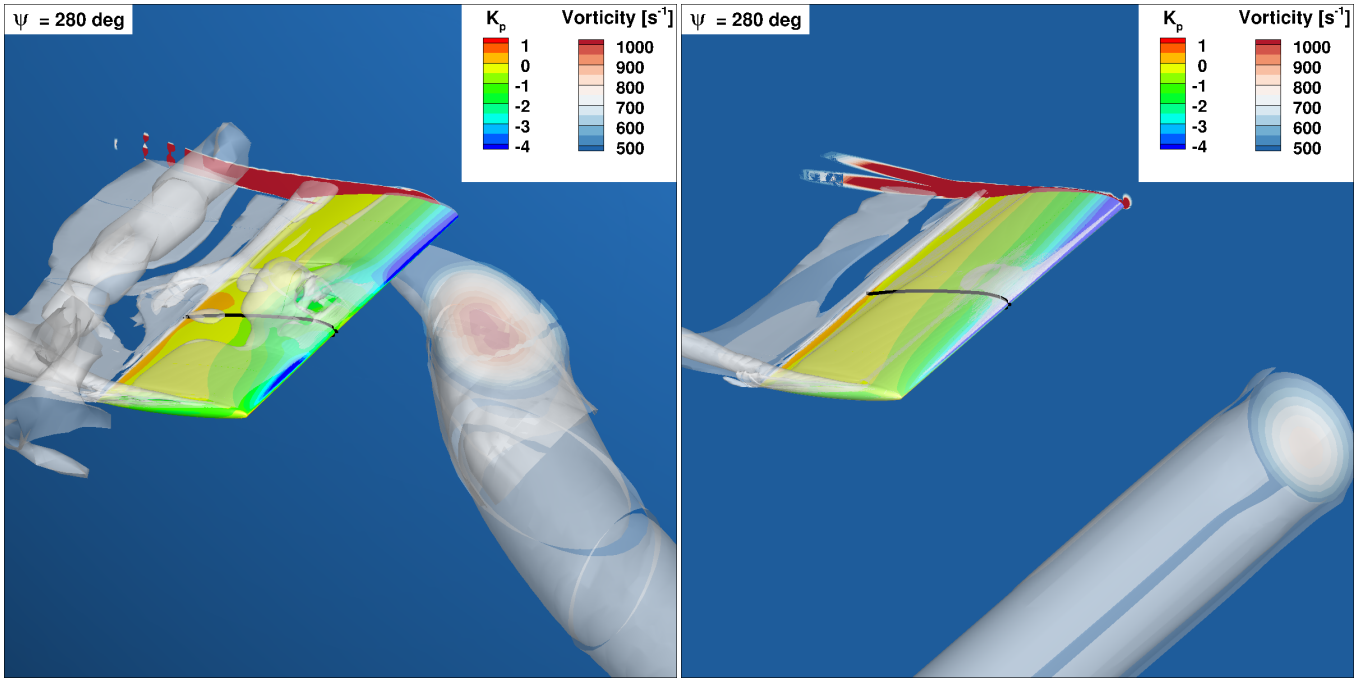

a) 3D HOST/*elsA* Simulation **b) 3D Simulation - Parallel BVI**

Figure 20: Vorticity field at $\psi = 280\,\text{deg}$ (MRPM).

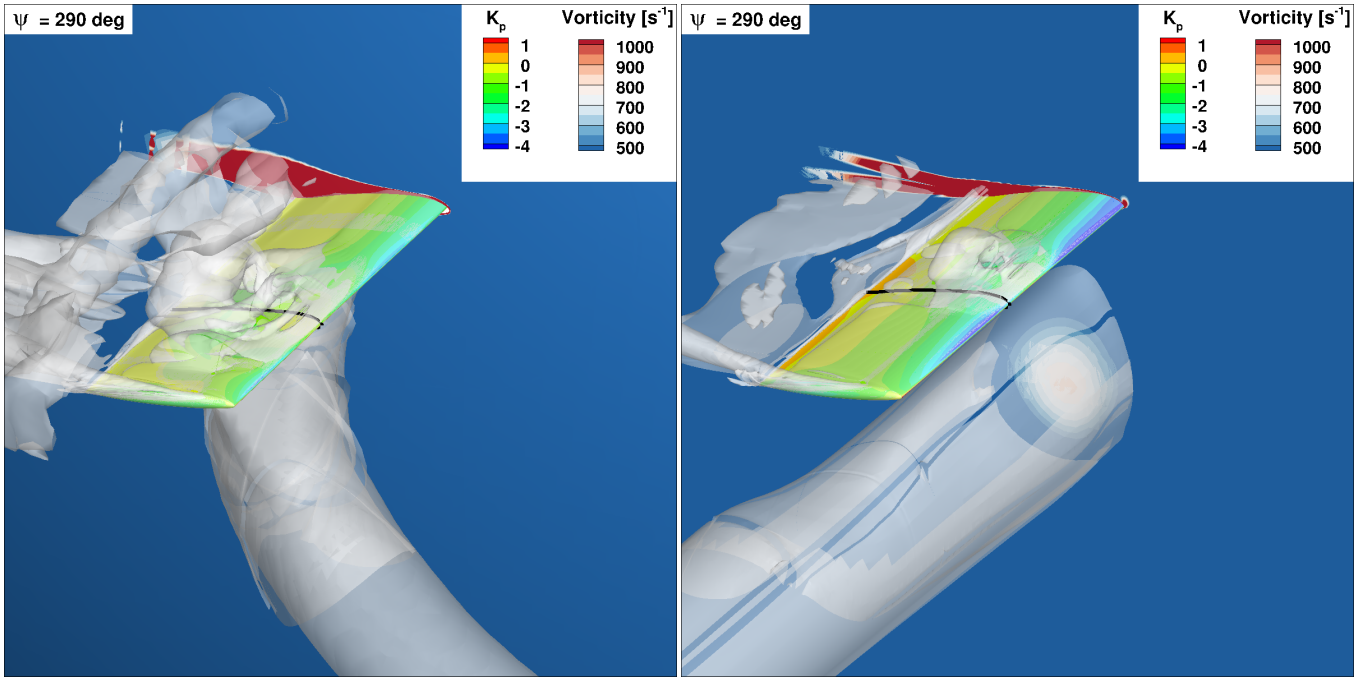

a) 3D HOST/*elsA* Simulation **b) 3D Simulation - Parallel BVI**

Figure 21: Vorticity field at $\psi = 290\,\text{deg}$ (MRPM).

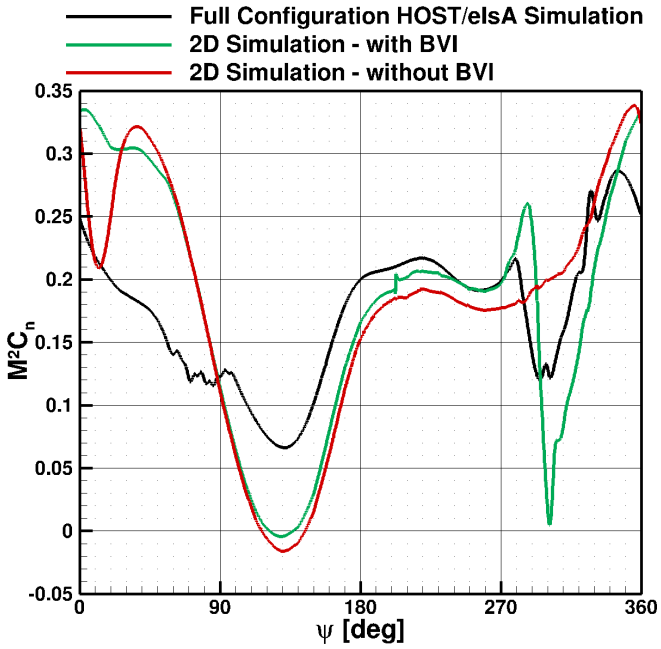

Figure 22: Sectional normal force coefficient of the MRPM case from 2D simulations with and without impacting vortex.

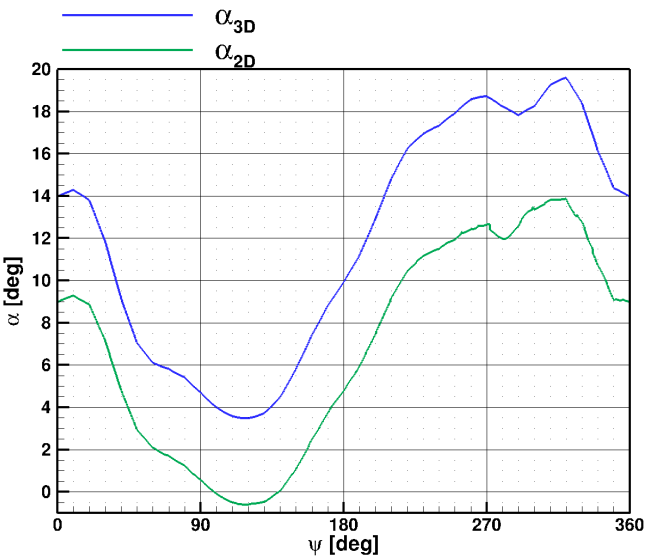

Figure 24: Angle of attack of the LRPM case used in 2D and 3D simulations.

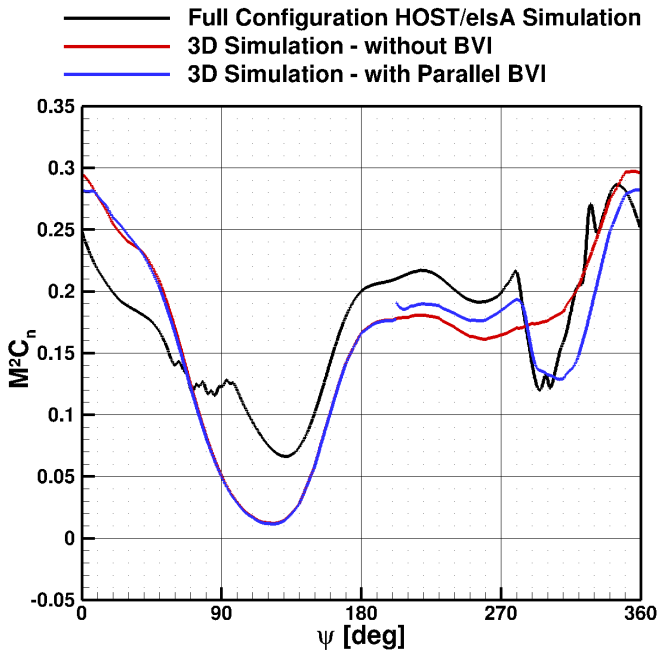

Figure 23: Sectional normal force coefficient of the MRPM case from 3D simulations with and without parallel impacting vortex.

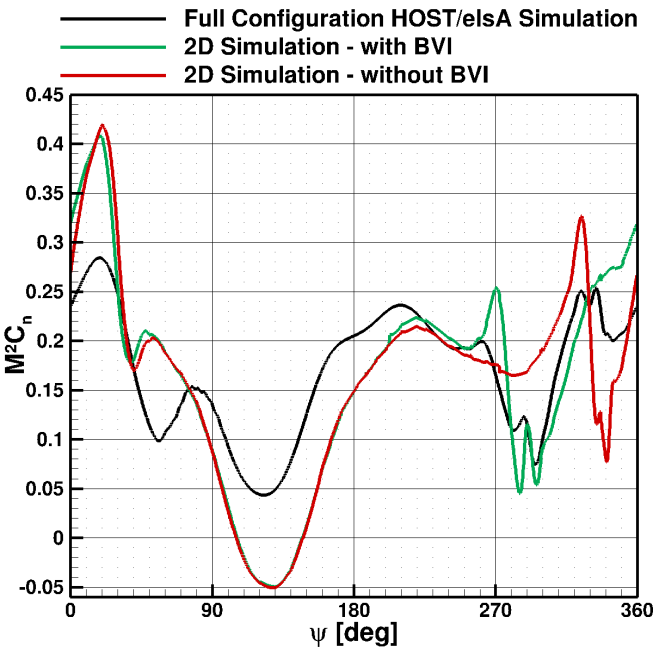

Figure 25: Sectional normal force coefficient of the LRPM case from 2D simulations with and without impacting vortex.

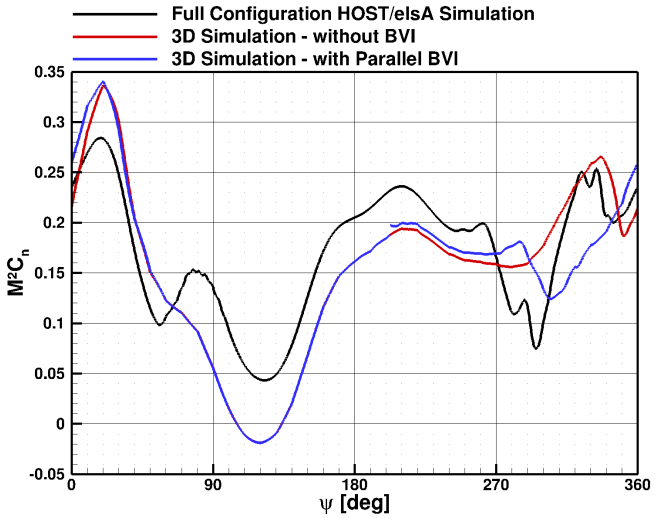

Figure 26: Sectional normal force coefficient of the LRPM case from 3D simulations with and without parallel impacting vortex.